

Floquet engineering Dirac bands in synthetic frequency lattices

Lingzhi Zheng,¹ Bing Wang^{1,*}, Chengzhi Qin,¹ Shuyue Chen,¹ Lange Zhao,¹ Shulin Wang,¹ Weiwei Liu,¹ and Peixiang Lu^{1,2}

¹*School of Physics and Wuhan National Laboratory for Optoelectronics, Huazhong University of Science and Technology, Wuhan 430074, China*

²*Hubei Key laboratory of Optical Information and Pattern Recognition, Wuhan Institute of Technology, Wuhan 430205, China*



(Received 24 July 2023; revised 6 October 2023; accepted 17 November 2023; published 21 December 2023)

A waveguide coupler under periodically cascaded dielectric modulation is proposed to generate a Floquet lattice in synthetic frequency dimension. The Floquet bands may hold linear in the entire Brillouin zone, referred to as Floquet Dirac bands and giving rise to nondiffracting frequency shifts. The direction of frequency shift depends on the component of incident transverse modes, analogous to the spin-momentum locking realized in driven ultracold atoms recently. Furthermore, the shape of Floquet bands can be flexibly adjusted by applying external modulation voltage, resulting in a tunable group velocity and diffraction coefficient. The discrete diffraction and dynamic localization are also demonstrated in the Floquet frequency lattice. The study provides a versatile platform to explore multiband Floquet lattice physics in synthetic dimensions, and may find applications in spectral manipulation, mode conversion, and mode-division demultiplexing.

DOI: [10.1103/PhysRevA.108.063515](https://doi.org/10.1103/PhysRevA.108.063515)

I. INTRODUCTION

Dirac points with linear band crossing in momentum space give rise to unconventional phenomena such as Klein tunneling and nondiffracting transport [1–4]. Dirac points in energy bands typically occur in special two-dimensional lattices such as graphene [5] and surface states of three-dimensional topological insulators [6]. Recently, a remarkable one-dimensional (1D) Dirac band with linear dispersion everywhere in the Brillouin zone has been experimentally demonstrated by ultracold atoms in optical lattices [7,8], which shows the one-to-one correspondence between the propagation direction of particles and their spin, namely the spin-momentum locking. The key concept to realize 1D Dirac bands is Floquet engineering, i.e., the control of systems using time-periodic perturbation. Floquet engineering has been demonstrated as a powerful tool to manipulate the properties of a system, especially the band structure [9,10]. A variety of nontrivial phenomena have been exhibited by using Floquet engineering, some of which are hard to realize or manipulate in static systems, such as 1D Floquet Dirac bands [7,8], Floquet topological insulators [9,11–13], anomalous π modes [14], discrete time crystals [15], beam rectifications [16], and dynamic localizations [17,18]. Most previous works in optical systems concerning Floquet engineering are limited in waveguide arrays where the propagation coordinate acts as time. The optical waveguide arrays can be manufactured by well-developed laser direct writing or etching technologies. However, the change of driving strength and frequency in waveguide arrays necessitates refabricating the device. Moreover, the fabrication is demanding and the size is relatively massive, which hinders their application feasibilities.

In contrast to waveguide arrays, synthetic frequency lattices are capable to construct controllable Floquet systems. The modes in an optical waveguide or ring resonator with evenly spaced frequencies couple to each other by applying dynamic refractive index modulation, forming a synthetic frequency lattice with tunable coupling strength and artificial gauge potential [19–23]. Synthetic frequency dimensions have enabled flexible experimental analogs of condensed-matter systems, and served as programmable photonic simulators for bosonic transport [24,25]. Higher-dimensional lattices can be implemented by applying multitone modulations [24,26–28] or adding the other dimensions, e.g., spatial dimension [29,30] and spin (orbital) angular momentum dimensions [31,32]. Numerous intriguing physical phenomena have been demonstrated in synthetic frequency dimensions, such as the quantum Hall effect [19], higher-order topological insulators [33], artificial non-Abelian gauge fields [34], non-Hermitian band braiding [35,36], and moiré lattices [37].

In this work, we demonstrate that coupled waveguides under periodically cascaded dielectric modulation are able to generate a Floquet frequency lattice. The Floquet driving strength can be controlled flexibly via external modulation voltage. Inspired by the spin-momentum locking induced by Floquet Dirac bands in driven ultracold atoms [7,8], we show that the Floquet frequency lattice can also exhibit Dirac bands which hold linear dispersion in the entire Brillouin zone. The supermodes in coupled waveguides act like pseudospins and the analogous spin-momentum locking can be realized. The frequency shifts are nondiffracting where the shift direction is corresponding to the type of incident supermodes. Furthermore, by changing the driving strength, the group velocity and diffraction coefficient of Floquet bands can be flexibly adjusted, leading to the phenomena of discrete diffraction and dynamic localization. The study provides a versatile platform to explore multiband physics of Floquet lattice in synthetic

*wangbing@hust.edu.cn

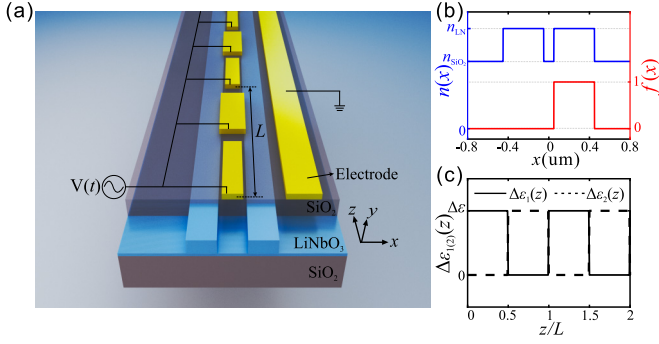


FIG. 1. (a) Schematic of coupled waveguides under periodically cascaded dynamic modulation. The system consists of two 400-nm-wide LiNbO₃ waveguides with 100-nm gap and the SiO₂ substrate. The periodically cascaded traveling-wave electrodes are composed of two segments with distinct geometries associated with different modulation wave numbers in one period L . (b) Transverse profiles of refractive index $n(x)$ and modulation $f(x)$. The refractive index for LiNbO₃ waveguides and SiO₂ substrate are $n_{\text{LN}} = 2.14$ and $n_{\text{SiO}_2} = 1.44$. (c) Profiles of modulation amplitude $\Delta\varepsilon_{1,2}(z)$ along propagation direction z .

dimensions, and may find applications in spectral manipulation, mode converters, and mode-division demultiplexing.

II. RESULTS AND DISCUSSION

A. Floquet frequency lattice

We start by considering a pair of coupled waveguides undergoing dynamic dielectric modulation as shown schematically in Fig. 1(a). The periodically cascaded traveling-wave modulations are composed of two alternate segments with distinct modulation wave numbers, which can be modeled by a modulated relative permittivity

$$\varepsilon_r(x, z, t) = \varepsilon_s + \Delta\varepsilon_1(z)f(x)\cos(\Omega t - q_1 z) + \Delta\varepsilon_2(z)f(x)\cos(\Omega t - q_2 z), \quad (1)$$

where ε_s denotes the static relative permittivity, while Ω , $q_{1,2}$, and $\Delta\varepsilon_{1,2}$ are modulation frequency, wave numbers, and amplitudes, respectively. The modulations are solely applied in the right waveguide, reflected by the modulation profile $f(x)$ as shown in Fig. 1(b). The periodically cascaded traveling-wave electrodes can be expressed by distance-varying modulation amplitudes as

$$\begin{aligned} \Delta\varepsilon_1(z) &= \Delta\varepsilon, & \Delta\varepsilon_2(z) &= 0, & z &\in [mL, mL + L/2) \\ \Delta\varepsilon_1(z) &= 0, & \Delta\varepsilon_2(z) &= \Delta\varepsilon, & z &\in [mL + L/2, (m+1)L), \end{aligned} \quad (2)$$

where m is an integer and $L/2$ is the length of an individual electrode. The modulation amplitude $\Delta\varepsilon$ should be a small perturbation compared to the static relative permittivity ε_s so that the disturbance to the wave numbers and mode profiles of even and odd modes can be ignored. As depicted in Fig. 1(c), the modulation amplitudes $\Delta\varepsilon_{1,2}$ accompanied by modulation wave numbers $q_{1,2}$ alternately switch on and off at $z = mL/2$, leading to a Floquet driving period L . The evanescent coupling between the fundamental modes in each waveguide gives rise

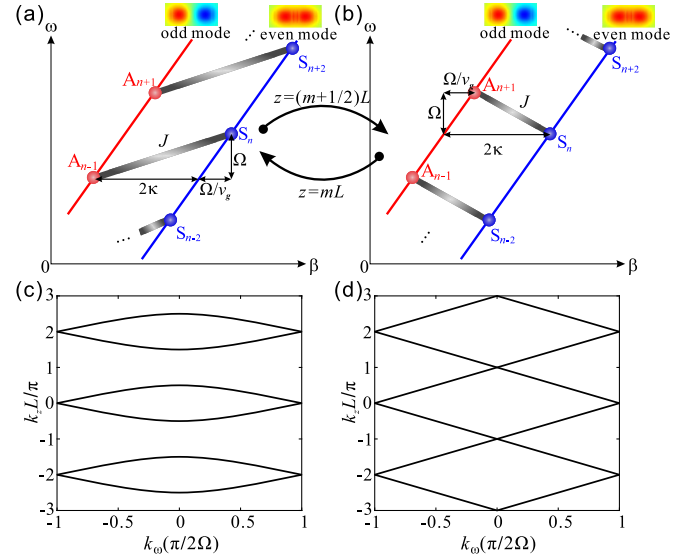


FIG. 2. (a), (b) Dispersion relation of coupled waveguides. The periodically dimerized coupling strengths between supermodes are induced by cascaded dynamic modulation and switch at $z = mL/2$, with m being an integer. (c), (d) Floquet energy bands for $LJ = \pi/2$ in (c) and $LJ = \pi$ in (d).

to the even and odd supermodes, forming a two-branch band as shown in Figs. 2(a) and 2(b). By applying cascaded dynamic dielectric modulation, the supermodes are coupled to form a Floquet frequency lattice. For concreteness, the electric field in the coupled waveguides can be expressed as

$$\begin{aligned} E(x, z, t) &= \sum_n S_n(z)\psi_S(x)\exp[i(\omega_n t - \beta_n^S z)] \\ &+ \sum_n A_n(z)\psi_A(x)\exp[i(\omega_n t - \beta_n^A z)], \end{aligned} \quad (3)$$

where S_n and A_n are mode amplitudes of even and odd supermodes with frequency $\omega_n = \omega_0 + n\Omega$ ($n = 0, \pm 1, \pm 2, \dots$), wave numbers $\beta_n^S = \beta_0^S + n\Omega/v_g$ and $\beta_n^A = \beta_0^A + n\Omega/v_g$, and eigenmode profile $\psi_{S(A)}$. Under low-frequency modulation $\Omega \ll \omega_0$, the slight distinction of eigenmode profile among different frequencies can be neglected and the dispersion can be regarded as linear given that the LiNbO₃ holds a low group-velocity dispersion $\text{GVD} = 112.19 \text{ fs}^2/\text{mm}$ (compared to Si as $\text{GVD} = 1119.4 \text{ fs}^2/\text{mm}$) at 1550 nm. The difference of wave numbers at the same frequency $\beta_n^S - \beta_n^A = 2\kappa$ is caused by evanescent coupling, where κ denotes the coupling strength which can be approximated to a constant under $\Omega \ll \omega_0$. The modulation wave numbers for the two segments of modulation are designed as

$$\begin{aligned} q_1 &= \Omega/v_g + 2\kappa \\ q_2 &= \Omega/v_g - 2\kappa, \end{aligned} \quad (4)$$

where v_g is the group velocity of the waveguide modes. Such design of modulation wave numbers induces the interband transitions between supermodes with evenly spaced frequencies as shown in Figs. 2(a) and 2(b). By substituting Eqs. (1)–(4) into Maxwell's equations, and using a slowly varying envelope approximation ($J \ll \beta_{S(A)}^n$) and

rotating wave approximation ($J \ll 4\kappa$) [21,38–40], we can derive the coupled-mode equation

$$\begin{aligned} i \frac{d}{dz} A_{n+1} &= J_1(z) S_{n+2} + J_2(z) S_n \\ i \frac{d}{dz} S_n &= J_1(z) A_{n-1} + J_2(z) A_{n+1}, \end{aligned} \quad (5)$$

and the corresponding coupling strengths

$$\begin{aligned} J_1(z) &= J, \quad J_2(z) = 0, \quad z \in [mL, mL + L/2) \\ J_1(z) &= 0, \quad J_2(z) = J, \quad z \in [mL + L/2, (m+1)L), \end{aligned} \quad (6)$$

where $J = \varepsilon_0 \int_{-\infty}^{\infty} f(x) \Delta \varepsilon \psi_A(x) \psi_S(x) dx / 8$ is independent with frequency given that the distinctions of eigenmode profile among different frequencies are neglected under low-frequency modulation, $\Omega \ll \omega_0$. Considering the parity of even and odd supermodes, an asymmetrical modulation profile $f(x)$ is enough to induce a nonvanishing coupling strength. As shown in Figs. 2(a) and 2(b), our frequency lattice mimics a Floquet lattice. The driving protocol consists of switching between two kinds of interband transition processes, with one between supermodes A_{n-1} and S_n during the first half period $[0, L/2) \pmod{L}$, and the other between S_n and A_{n+1} during the second half period $[L/2, L) \pmod{L}$. The Floquet driving strength J , associated with modulation strength $\Delta \varepsilon$, can be flexibly tuned via external modulation voltage without refabricating a new device. The controllable Floquet frequency lattice provides a versatile platform for demonstrating the physical phenomena of Floquet lattices. As an example, we will show the Floquet Dirac bands with linear dispersion everywhere in the Brillouin zone and the analogous spin-momentum locking in the following.

B. Floquet Dirac band and spin-momentum locking

The properties of stroboscopic dynamics of Floquet lattice systems are reflected in Floquet bands [10]. By defining $A_{2n-1}(S_{2n}) = \int_{\text{BZ}} dk_\omega A_{k_\omega}(S_{k_\omega}) \exp[2ik_\omega n \Omega]$, where k_ω denotes the Bloch wave number in frequency dimension, the coupled-mode equation in k space corresponding to Eq. (5) is

$$\begin{aligned} i \frac{d}{dz} \begin{bmatrix} A_{k_\omega} \\ S_{k_\omega} \end{bmatrix} &= \begin{bmatrix} 0 & J_1(z) + J_2(z) e^{-2ik_\omega \Omega} \\ J_1(z) + J_2(z) e^{2ik_\omega \Omega} & 0 \end{bmatrix} \\ &\times \begin{bmatrix} A_{k_\omega} \\ S_{k_\omega} \end{bmatrix}, \end{aligned} \quad (7)$$

which defines the Hamiltonians associated with two respective half periods

$$H_1 = \begin{bmatrix} 0 & J \\ J & 0 \end{bmatrix}, \quad H_2 = \begin{bmatrix} 0 & J e^{-2ik_\omega \Omega} \\ J e^{2ik_\omega \Omega} & 0 \end{bmatrix} \quad (8)$$

and gives rise to the single-period evolution operator

$$U_k(L) = e^{-iH_2 L/2} e^{-iH_1 L/2} \quad (9)$$

Hence, the Floquet Hamiltonian H_F , defined as $\exp(-iH_F L) = U_k(L)$, is a stationary effective Hamiltonian that describes the stroboscopic evolution of the system after each driving period. The Floquet bands are the eigenvalues of

H_F , which are found to be

$$k_z = \pm \frac{1}{L} \arccos[\cos^2(LJ/2) - \sin^2(LJ/2) \cos(2k_\omega \Omega)] \quad (10)$$

The Floquet bands are depicted in Fig. 2(c), which shows a two-band structure and a degeneracy in the boundary of Brillouin zone. In particular, for $LJ = \pi$, the Floquet bands become linear everywhere in the Brillouin zone, i.e., an ideal realization of the 1D Dirac fermion, as shown in Fig. 2(d). Therefore, the nondiffracting transports can be realized with arbitrary excited Bloch states, unlike the typical Dirac semimetals such as graphene, in which the linear dispersion only exists in the vicinity of Dirac points, leading to a nondiffracting transport associated with specific Bloch momentum.

The nondiffracting transports in the proposed Floquet systems are accompanied by spin-momentum locking. We can compute the Floquet Hamiltonian for $LJ = \pi$ as

$$H_F(k_\omega) = (1/L) 2k_\omega \Omega \sigma_z + \pi/L, \quad (11)$$

where σ_z denotes the third standard Pauli matrix. Such Hamiltonian mimics a Dirac fermion with positive (negative) velocity for up (down) spin. As mentioned before, the Floquet Hamiltonian describes the stroboscopic evolution of the system after each driving period. However, the so-called micromotion within a period is hidden [41], i.e., the spins are allowed to change during the period, but must recover themselves after each period. In our systems, the odd and even supermodes play the role of up and down spins, respectively, and the velocity of frequency shift is the analog of momentum. The spin-momentum locking implies that the input even (odd) supermodes will undergo red (blue) shift with nondiffraction in the frequency domain. We simulated the nondiffracting frequency shifts by first-principle simulations using the 2D finite-difference time-domain (FDTD) method. As demonstrated by the field distribution in Fig. 3(a) and the spectral evolutions of even and odd modes in Figs. 3(b) and 3(c), the excited even mode manifests redshift without frequency diffraction. The nondiffracting blueshift for odd-mode excitation is shown in Figs. 3(d)–3(f). The black circles in spectra are solved by coupled-mode Eq. (5), which shows good agreement with the first-principle simulated spectra denoted by red and blue lines. Such a phenomenon can be understood at an intuitive level. Under $LJ = \pi$, the amplitudes between adjacent coupled sites are completely exchanged in each half period. Therefore, in the first half period as shown in Fig. 2(a), the excited even-mode S_0 is fully transferred into odd-mode A_{-1} . For the second half period as shown in Fig. 2(b), the odd-mode A_{-1} recovers to even mode and accompanies redshift to S_{-2} . These processes repeat in the subsequent periods, leading to the nondiffracting redshift. The switches of transverse modes are demonstrated by field distribution in Fig. 3(a), and the nondiffracting redshift is shown by spectral evolutions of even and odd modes in Figs. 3(b) and 3(c). The tiny diffractions in Figs. 3(b) and 3(c) are caused by group-velocity dispersion. The GVD leads to the wave number mismatching between waveguide coupler and modulation, i.e., the deviation from Eq. (4), and further induces the incomplete mode conversion. Similar analyses can be applied to the case of odd-mode excitations, which undergo

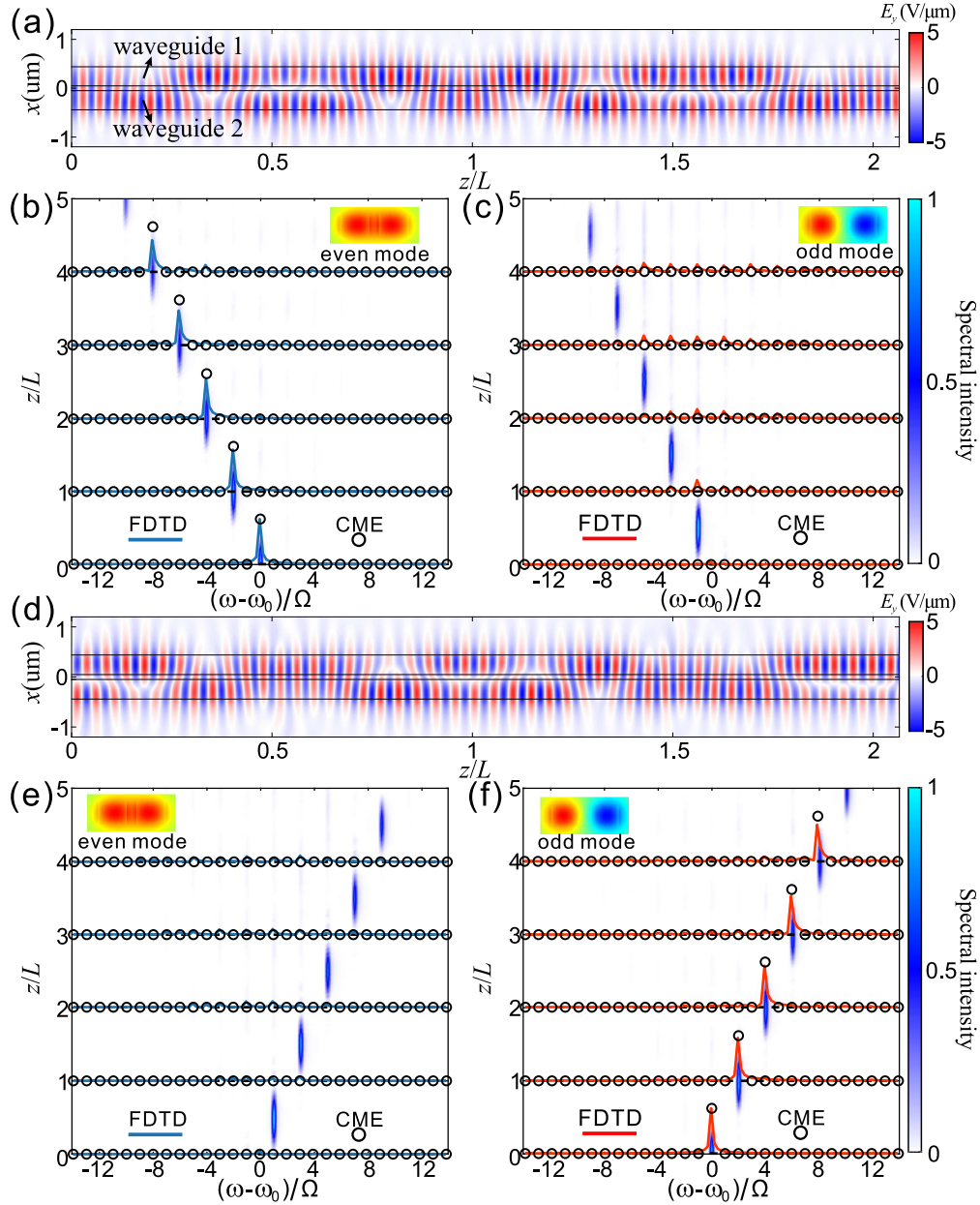


FIG. 3. Spin-momentum locking with monochromatic excitation. (a)–(c) Distribution of electric fields (a) and corresponding spectral evolutions for even mode (b) and odd mode (c) with monochromatic even-mode excitation under $LJ = \pi$. The blue(red) lines are the even(odd) modes spectra solved by FDTD method and black circles are solved by the coupled-mode Eq. (5). The shaded areas in (b) and (c) indicate the spectral intensity of even and odd modes calculated by FDTD method and normalized to the intensity of excited light. (d)–(f) Distribution of electric fields and corresponding spectral evolutions with monochromatic odd-mode excitation under $LJ = \pi$. The modulation frequency is $f = \Omega/2\pi = 1$ THz. The modulation amplitude is $\Delta\epsilon = 0.4 \times n_{LN}$ for $LJ = \pi$. The length for one driving period of cascaded dynamic modulation is $L = 18 \mu\text{m}$. The wavelength of excited light is 1550 nm .

blueshifts without diffraction in the frequency domain. It is worth noting that input position will affect the direction of frequency shift of even and odd modes. For instance, the even (odd) modes will undergo blue (red) shift if the source is put at $z = L/2$. The FDTD update equations with time-varying permittivity can be found in Ref. [42]. We consider the TE modes (E_y , H_z , H_x) of the waveguides. The boundary is set as convolutional perfectly matched layer [43]. The parameters related to modulation wave numbers are $\Omega/v_g = 0.0391 \mu\text{m}^{-1}$ and $\kappa = 0.4341 \mu\text{m}^{-1}$.

The spin-momentum locking in the Floquet frequency lattice is useful for mode-division multiplexing applications. We simulated the spectral evolutions by the FDTD method with frequency comb excitation as shown in Figs. 4(a) and 4(b). The excited frequency combs contain both even and odd modes which can be expressed as

$$E(x, z = 0, t) = \sum_n \psi_S(x) e^{-n^2/D_S^2} e^{i\omega_n t} + \sum_n \psi_A(x) e^{-n^2/D_A^2} e^{i\omega_n t}, \quad (12)$$

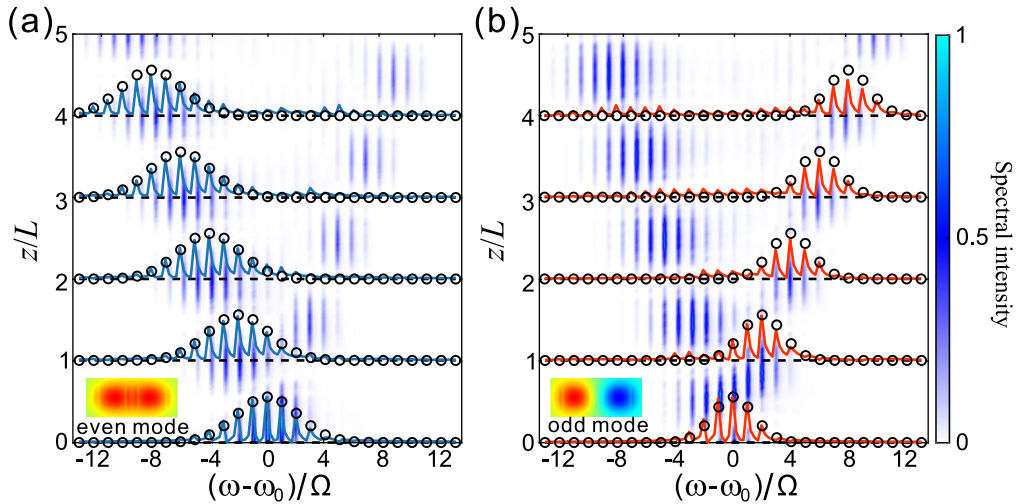


FIG. 4. Spin-momentum locking with frequency comb excitation. (a), (b) Spectral evolutions for even modes in (a) and odd modes in (b) with mixed supermodes frequency comb excitation under $LJ = \pi$.

where the mode amplitudes for even and odd supermodes are Gaussian distribution in spectra with different widths as $D_S = 3$ and $D_A = 2$. The incident even and odd modes manifest non-diffracting red- and blueshifts respectively, i.e., the frequency combs are separated in spectra according to the type of input supermodes. Therefore, the information encoded in supermodes is separated in the frequency domain which can be used for demultiplexing. The condition for spin-momentum locking $LJ = \pi$ is practically accessible given that the coupling strength J can be flexibly adjusted by external modulation voltage, which enables the device to work in a controllable manner.

C. Discrete diffraction and dynamical localization

The dynamic of the Floquet lattice can be characterized by the group velocity $v_{k\omega} = dk_z/dk_\omega$ and diffraction coefficient $D_{k\omega} = d^2 k_z/dk_\omega^2$. In frequency lattice, they indicate the velocity of frequency shift and bandwidth expansion. Figure 5(a) depicts the maximum group velocity and the diffraction coefficient of the Floquet band as coupling strength J varies. The diffraction coefficient is supposed to take the maximum at $k_\omega = 0$. However, we choose it at $k_\omega = \pi/4\Omega$ in Fig. 5(a) to avoid the ambiguous definition when the degeneracy occurs. Unlike the nondriving lattice in which the group velocity and diffraction coefficient grow with coupling strength, they behave periodically in the Floquet lattice. Such properties are also demonstrated by the output spectra corresponding to different coupling strength J as shown in Fig. 5(b), in which the excited even mode at central frequency S_0 undergoes ten driving periods. The output spectra pattern varies periodically with coupling strength as predicted in Fig. 5(a). In general, the Floquet bands are dispersive. For instance, as $LJ = \pi/2$, the Floquet bands are bent as shown in Fig. 2(c) with both finite group velocity and diffraction coefficient. We simulated the field distribution and the spectral evolutions of even and odd modes by the FDTD method as shown in Figs. 6(a)–6(c). The electric field is generally composed of both even and odd modes and the spectral evolutions ex-

hibit discrete diffraction. However, at $LJ = n\pi$ ($n = 0, 1, 2, \dots$), the diffraction coefficient vanishes, which indicates the nondiffracting transport. For example, as $LJ = \pi$, the Floquet band hosts vanished diffraction coefficient and nonzero group velocity, which corresponds to the Floquet Dirac band exhibiting nondiffracting directional frequency shift. The non-diffracting redshift with monochromatic even-mode excitation

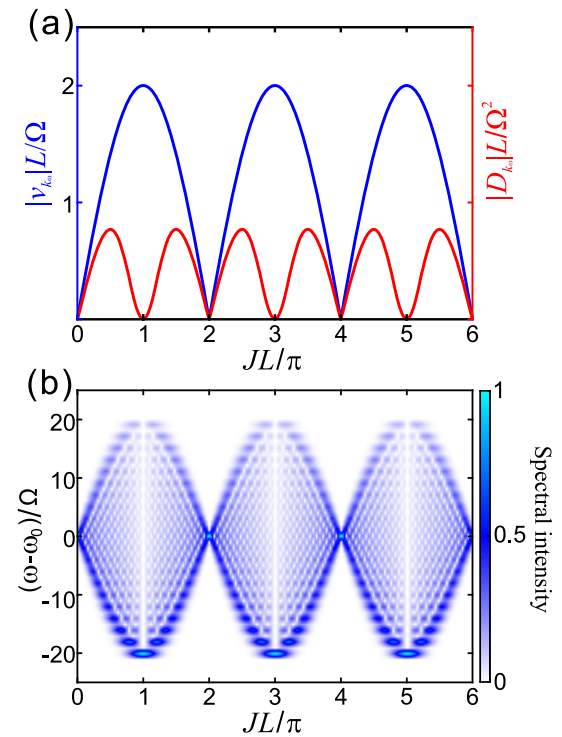


FIG. 5. (a) Maximum group velocity $|v_{k\omega}|$ and diffraction coefficient $|D_{k\omega}|$ for $k_\omega = \pi/4\Omega$ under different coupling strength J . (b) Output frequency spectrum vs coupling strength J with monochromatic even-mode excitation at 1550 nm. The length of modulation region contains ten driving periods.

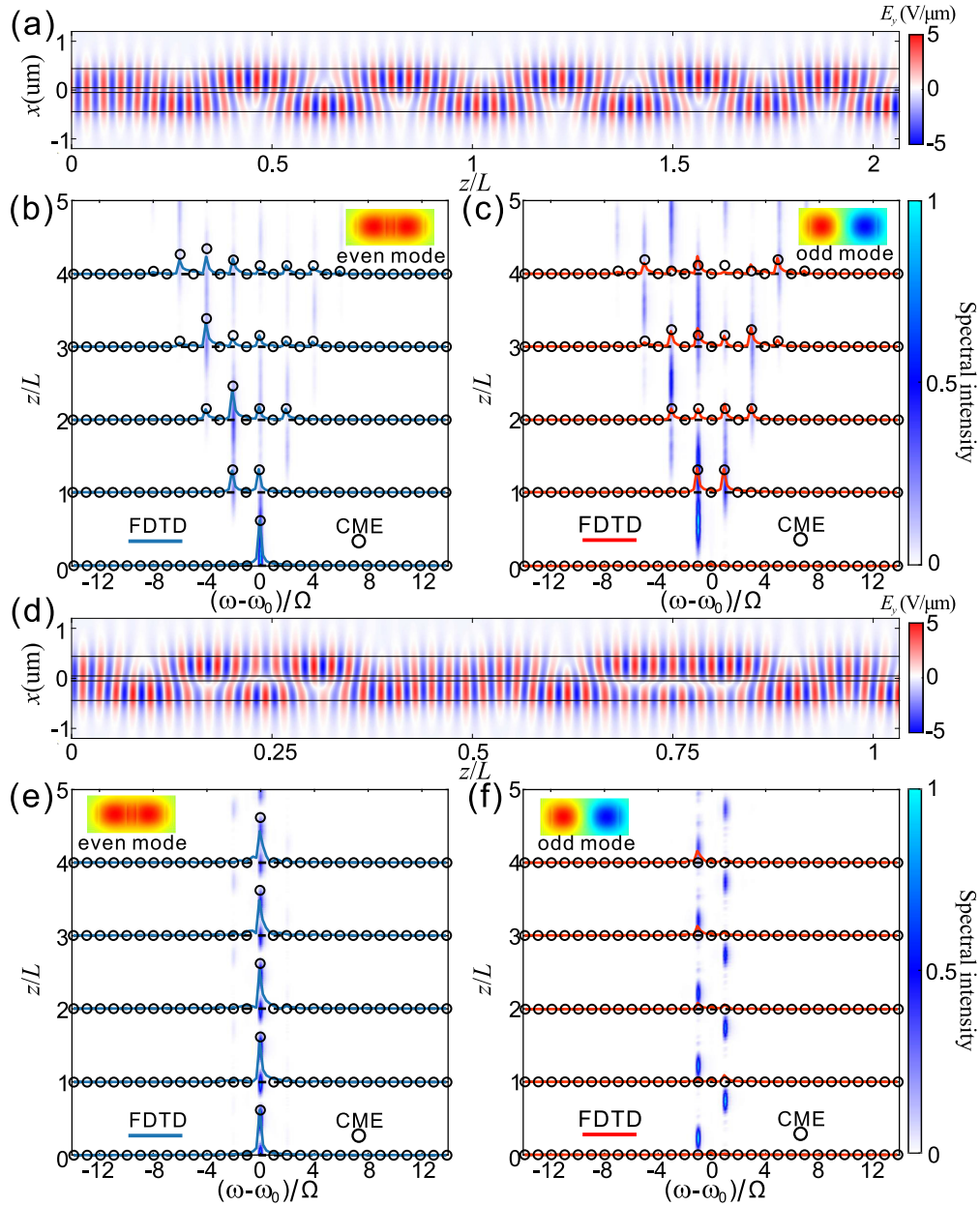


FIG. 6. Discrete diffraction and dynamic localization. (a)–(c) Distribution of electric fields (a) and corresponding spectral evolutions for even mode (b) and odd mode (c) with monochromatic even-mode excitation under $LJ = \pi/2$. (d)–(f) Distribution of electric fields and corresponding spectral evolutions under $LJ = 2\pi$. The modulation frequency is $f = \Omega/2\pi = 1$ THz. The other parameters are $\Delta\varepsilon = 0.2 \times n_{LN}$ and $L = 18 \mu\text{m}$ for (a)–(c), and $\Delta\varepsilon = 0.4 \times n_{LN}$ and $L = 36 \mu\text{m}$ for (d)–(f). The wavelength of excited light is 1550 nm.

is demonstrated in Figs. 3(a)–3(c) and agrees with the asymmetric pattern in Fig. 5(b). Intriguingly, when the coupling strength increases to $LJ = 2\pi$, the diffraction coefficient vanishes once again but accompanies zero group velocity. The Floquet bands turn out to be flat as $k_z = 0$ according to Eq. (10). Intuitively, the incident supermodes are fully transformed into adjacent sites and back in half-driving period, i.e., they undergo a complete Rabi oscillation period. This process repeats in the following evolution, leading to the phenomenon of dynamic localization. As shown in Figs. 6(d)–6(f), the excited even-mode S_0 is transferred to A_{-1} at $z = L/4$ and then comes back to S_0 at $z = L/2$. In the next half period,

it undergoes transitions as $S_0 \rightarrow A_1 \rightarrow S_0$. Therefore, the frequency mode is invariant after a driving period. The further larger coupling strength will not induce larger group velocity, which only results in additional Rabi oscillation processes in a driving period. For instance, when $LJ = 3\pi$, the input supermodes undergo $1/2$ Rabi oscillation processes in half driving period, which is equivalent to the case $LJ = \pi$. For $LJ = 4\pi$, the supermodes undergo the Rabi oscillation process twice in half driving period, leading to dynamic localization analogous to the case $LJ = 2\pi$. It is worth noting that the coupling strength can be flexibly adjusted by external modulation and a long-distance modulation with a small modulation amplitude

can also lead to a significant phase modulation depth LJ . Therefore, the property of frequency diffraction and the corresponding output spectrum can be conveniently manipulated in practice.

III. CONCLUSIONS

In summary, we constructed a Floquet frequency lattice by a waveguide coupler under periodically cascaded dielectric modulation. The Floquet band may show linear dispersion in the entire Brillouin zone, referred to as Floquet Dirac band. The nondiffracting frequency shift is realized and the shift directions are determined by the transverse modes of incident light, mimicking the spin-momentum locking in ultracold atom lattices. The supermode frequency comb can be excited by using an asymmetric directional coupler from different ports experimentally [44,45]. We also demonstrated the discrete diffraction and dynamic localization by adjusting the coupling strength, which can be flexibly controlled by external modulation voltage. The results in our work are available for lower-modulation frequency which is experimentally feasible. For instance, the integrated LN electro-optic modulator has

high bandwidths (>100 GHz) and possesses ultralow on-chip optical losses which provides an ideal experimental platform for realizing the Floquet frequency lattice [46]. The proposed systems are compatible with state-of-the-art integrated thin-film lithium niobate platform [47] or silicon chip [48], and the physical implementation can be based on traveling-wave electrodes [46,49] or placing pn -junction electrical diodes inside silicon waveguides [50,51]. It is worth noting that the synthetic frequency lattice can be created with the nonlinear process of four-wave mixing Bragg scattering and the bandwidth of frequency manipulation is expanded up to terahertz as experimentally demonstrated [20,52]. Our system provides a versatile platform for demonstrating physical phenomena of Floquet lattice in synthetic dimensions, and has potential application in mode converters, spectral manipulation, and mode-division demultiplexing.

ACKNOWLEDGMENT

This work was supported by the National Natural Science Foundation of China (Grants No. 12374305, No. 11974124, No. 12021004, No. 12147151, and No. 12204185).

-
- [1] A. H. Castro Neto, F. Guinea, N. M. R. Peres, K. S. Novoselov, and A. K. Geim, The electronic properties of graphene, *Rev. Mod. Phys.* **81**, 109 (2009).
 - [2] J. M. Zeuner, N. K. Efremidis, R. Keil, F. Dreisow, D. N. Christodoulides, A. Tünnermann, S. Nolte, and A. Szameit, Optical analogues for massless Dirac particles and conical diffraction in one dimension, *Phys. Rev. Lett.* **109**, 023602 (2012).
 - [3] M. I. Katsnelson, K. S. Novoselov, and A. K. Geim, Chiral tunnelling and the Klein paradox in graphene, *Nat. Phys.* **2**, 620 (2006).
 - [4] M. Hu, K. Ding, T. Qiao, X. Jiang, Q. Wang, S. Zhu, and H. Liu, Realization of photonic charge-2 Dirac point by engineering super-modes in topological superlattices, *Commun. Phys.* **3**, 130 (2020).
 - [5] A. K. Geim, Graphene: Status and prospects, *Science* **324**, 1530 (2009).
 - [6] M. Z. Hasan and C. L. Kane, Colloquium: Topological insulators, *Rev. Mod. Phys.* **82**, 3045 (2010).
 - [7] J. C. Budich, Y. Hu, and P. Zoller, Helical Floquet channels in 1D lattices, *Phys. Rev. Lett.* **118**, 105302 (2017).
 - [8] M. Lu, G. H. Reid, A. R. Fritsch, A. M. Pineiro, and I. B. Spielman, Floquet engineering topological Dirac bands, *Phys. Rev. Lett.* **129**, 040402 (2022).
 - [9] M. S. Rudner and N. H. Lindner, Band structure engineering and non-equilibrium dynamics in Floquet topological insulators, *Nat. Rev. Phys.* **2**, 229 (2020).
 - [10] T. Oka and S. Kitamura, Floquet engineering of quantum materials, *Annu. Rev. Condens. Matter Phys.* **10**, 387 (2019).
 - [11] L. J. Maczewsky, J. M. Zeuner, S. Nolte, and A. Szameit, Observation of photonic anomalous Floquet topological insulators, *Nat. Commun.* **8**, 13756 (2017).
 - [12] S. Mukherjee, A. Spracklen, M. Valiente, E. Andersson, P. Ohberg, N. Goldman, and R. R. Thomson, Experimental observation of anomalous topological edge modes in a slowly driven photonic lattice, *Nat. Commun.* **8**, 13918 (2017).
 - [13] E. Lustig, S. Weimann, Y. Plotnik, Y. Lumer, M. A. Bandres, A. Szameit, and M. Segev, Photonic topological insulator in synthetic dimensions, *Nature (London)* **567**, 356 (2019).
 - [14] Q. Cheng, Y. Pan, H. Wang, C. Zhang, D. Yu, A. Gover, H. Zhang, T. Li, L. Zhou, and S. Zhu, Observation of anomalous π modes in photonic Floquet engineering, *Phys. Rev. Lett.* **122**, 173901 (2019).
 - [15] H. Taheri, A. B. Matsko, L. Maleki, and K. Sacha, All-optical dissipative discrete time crystals, *Nat. Commun.* **13**, 848 (2022).
 - [16] F. Dreisow, Y. V. Kartashov, M. Heinrich, V. A. Vysloukh, A. Tünnermann, S. Nolte, L. Torner, S. Longhi, and A. Szameit, Spatial light rectification in an optical waveguide lattice, *Europhys. Lett.* **101**, 44002 (2013).
 - [17] Y. V. Kartashov, V. A. Vysloukh, V. V. Konotop, and L. Torner, Diffraction control in PT-symmetric photonic lattices: From beam rectification to dynamic localization, *Phys. Rev. A* **93**, 013841 (2016).
 - [18] S. Wang, C. Qin, W. Liu, B. Wang, F. Zhou, H. Ye, L. Zhao, J. Dong, X. Zhang, S. Longhi *et al.*, High-order dynamic localization and tunable temporal cloaking in ac-electric-field driven synthetic lattices, *Nat. Commun.* **13**, 7653 (2022).
 - [19] L. Yuan, Y. Shi, and S. Fan, Photonic gauge potential in a system with a synthetic frequency dimension, *Opt. Lett.* **41**, 741 (2016).
 - [20] B. A. Bell, K. Wang, A. S. Solntsev, D. N. Neshev, A. A. Sukhorukov, and B. J. Eggleton, Spectral photonic lattices with complex long-range coupling, *Optica* **4**, 1433 (2017).
 - [21] C. Qin, F. Zhou, Y. Peng, D. Sounas, X. Zhu, B. Wang, J. Dong, X. Zhang, A. Alu, and P. Lu, Spectrum control through

- discrete frequency diffraction in the presence of photonic gauge potentials, *Phys. Rev. Lett.* **120**, 133901 (2018).
- [22] L. Yuan, Q. Lin, M. Xiao, and S. Fan, Synthetic dimension in photonics, *Optica* **5**, 1396 (2018).
- [23] L. Yuan, A. Dutt, and S. Fan, Synthetic frequency dimensions in dynamically modulated ring resonators, *APL Photonics* **6**, 071102 (2021).
- [24] A. Senanian, L. G. Wright, P. F. Wade, H. K. Doyle, and P. L. McMahon, Programmable large-scale simulation of bosonic transport in optical synthetic frequency lattices, *Nat. Phys.* **19**, 1333 (2023).
- [25] U. A. Javid, R. Lopez-Rios, J. Ling, A. Graf, J. Staffa, and Q. Lin, Chip-scale simulations in a quantum-correlated synthetic space, *Nat. Photon.* **17**, 883 (2023).
- [26] Y. Hu, C. Reimer, A. Shams-Ansari, M. Zhang, and M. Loncar, Realization of high-dimensional frequency crystals in electro-optic microcombs, *Optica* **7**, 1189 (2020).
- [27] Z. Liu, L. Zheng, C. Qin, B. Wang, and P. Lu, Multidimensional synthetic frequency lattice in the dynamically modulated waveguides, *Opt. Lett.* **48**, 3163 (2023).
- [28] D. Cheng, E. Lustig, K. Wang, and S. Fan, Multi-dimensional band structure spectroscopy in the synthetic frequency dimension, *Light Sci. Appl.* **12**, 158 (2023).
- [29] Q. Lin, X.-Q. Sun, M. Xiao, S.-C. Zhang, and S. Fan, A three-dimensional photonic topological insulator using a two-dimensional ring resonator lattice with a synthetic frequency dimension, *Sci. Adv.* **4**, eaat2774 (2018).
- [30] Y. Song, W. Liu, L. Zheng, Y. Zhang, B. Wang, and P. Lu, Two-dimensional non-Hermitian skin effect in a synthetic photonic lattice, *Phys. Rev. Appl.* **14**, 064076 (2020).
- [31] A. Dutt, Q. Lin, L. Yuan, M. Minkov, M. Xiao, and S. Fan, A single photonic cavity with two independent physical synthetic dimensions, *Science* **367**, 59 (2020).
- [32] L. Yuan, Q. Lin, A. Zhang, M. Xiao, X. Chen, and S. Fan, Photonic gauge potential in one cavity with synthetic frequency and orbital angular momentum dimensions, *Phys. Rev. Lett.* **122**, 083903 (2019).
- [33] A. Dutt, M. Minkov, I. A. D. Williamson, and S. Fan, Higher-order topological insulators in synthetic dimensions, *Light Sci. Appl.* **9**, 131 (2020).
- [34] D. Cheng, K. Wang, and S. Fan, Artificial non-Abelian lattice gauge fields for photons in the synthetic frequency dimension, *Phys. Rev. Lett.* **130**, 083601 (2023).
- [35] K. Wang, A. Dutt, C. C. Wojcik, and S. Fan, Topological complex-energy braiding of non-Hermitian bands, *Nature (London)* **598**, 59 (2021).
- [36] K. Wang, A. Dutt, K. Y. Yang, C. C. Wojcik, J. Vučković, and S. Fan, Generating arbitrary topological windings of a non-Hermitian band, *Science* **371**, 1240 (2021).
- [37] D. Yu, G. Li, L. Wang, D. Leykam, L. Yuan, and X. Chen, Moiré lattice in one-dimensional synthetic frequency dimension, *Phys. Rev. Lett.* **130**, 143801 (2023).
- [38] Z. Yu and S. Fan, Complete optical isolation created by indirect interband photonic transitions, *Nat. Photon.* **3**, 91 (2009).
- [39] K. Fang, Z. Yu, and S. Fan, Photonic Aharonov-Bohm effect based on dynamic modulation, *Phys. Rev. Lett.* **108**, 153901 (2012).
- [40] L. Zheng, B. Wang, C. Qin, L. Zhao, S. Chen, W. Liu, and P. Lu, Chiral Zener tunneling in non-Hermitian frequency lattices, *Opt. Lett.* **47**, 4644 (2022).
- [41] F. Harper, R. Roy, M. S. Rudner, and S. L. Sondhi, Topology and broken symmetry in Floquet systems, *Annu. Rev. Condens. Matter Phys.* **11**, 345 (2020).
- [42] L. Zeng, J. Xu, C. Wang, J. Zhang, Y. Zhao, J. Zeng, and R. Song, Photonic time crystals, *Sci. Rep.* **7**, 17165 (2017).
- [43] J. A. Roden and S. D. Gedney, Convolution PML (CPML): An efficient FDTD implementation of the CFS-PML for arbitrary media, *Microw. Opt. Technol. Lett.* **27**, 334 (2000).
- [44] C. Li, D. Liu, and D. Dai, Multimode silicon photonics, *Nanophotonics* **8**, 227 (2018).
- [45] Q. Liu, S. Li, B. Wang, S. Ke, C. Qin, K. Wang, W. Liu, D. Gao, P. Berini, and P. Lu, Efficient mode transfer on a compact silicon chip by encircling moving exceptional points, *Phys. Rev. Lett.* **124**, 153903 (2020).
- [46] C. Wang, M. Zhang, X. Chen, M. Bertrand, A. Shams-Ansari, S. Chandrasekhar, P. Winzer, and M. Loncar, Integrated lithium niobate electro-optic modulators operating at CMOS-compatible voltages, *Nature (London)* **562**, 101 (2018).
- [47] A. Boes, L. Chang, C. Langrock, M. Yu, M. Zhang, Q. Lin, M. Loncar, M. Fejer, J. Bowers, and A. Mitchell, Lithium niobate photonics: Unlocking the electromagnetic spectrum, *Science* **379**, eabj4396 (2023).
- [48] N. Margalit, C. Xiang, S. M. Bowers, A. Bjorlin, R. Blum, and J. E. Bowers, Perspective on the future of silicon photonics and electronics, *Appl. Phys. Lett.* **118**, 220501 (2021).
- [49] M. Zhang, C. Wang, P. Kharel, D. Zhu, and M. Loncar, Integrated lithium niobate electro-optic modulators: When performance meets scalability, *Optica* **8**, 652 (2021).
- [50] H. Lira, Z. Yu, S. Fan, and M. Lipson, Electrically driven nonreciprocity induced by interband photonic transition on a silicon chip, *Phys. Rev. Lett.* **109**, 033901 (2012).
- [51] L. D. Tzauang, K. Fang, P. Nussenzeig, S. Fan, and M. Lipson, Non-reciprocal phase shift induced by an effective magnetic flux for light, *Nat. Photonics* **8**, 701 (2014).
- [52] W. Li, N. Yang, H. Chen, B. Wang, C. Qin, T. Han, Y. Zhang, W. Liu, C. Zhang, X. Zhang *et al.*, Broadband frequency control of light using synthetic frequency lattices formed by four-wave-mixing Bragg scatterings, *Phys. Rev. A* **103**, 033514 (2021).